Sb doped SnO₂-decorated porous *g*-C₃N₄ nanosheet heterostructures with enhanced photocatalytic activities under visible light irradiation

Liuqing Yang[a,b], Jianfeng Huang[a,*], Li Shi[b], Liyun Cao[a], Huimin Liu[b], Yanyu Liu[c], Yunxiang Li[b], Hui Song[b], Yanni Jie[a], Jinhua Ye[b,d,e,**]

[a] *School of Materials Science and Engineering, Shaanxi University of Science and Technology, Weiyang, Xi'an, Shaanxi 710021, PR China*
[b] *International Center for Materials Nanoarchitectomics (WPI-MANA), National Institute for Materials Science (NIMS), 1-1 Namiki, Tsukuba, Ibaraki 305-0044, Japan*
[c] *Department of Applied Physics, Tianjin Key Laboratory of Low Dimensional Materials Physics and Preparing Technology, Faculty of Science, Tianjin University, Tianjin, 300072, PR China*
[d] *TU-NIMS International Collaboration Laboratory, School of Materials Science and Engineering, Tianjin University, 92 Weijin Road, Nankai District, Tianjin, 300072, PR China*
[e] *Collaborative Innovation Center of Chemical Science and Engineering (Tianjin), Tianjin, 300072, PR China*

ARTICLE INFO

ABSTRACT

A novel Sb doped SnO₂ decorated porous *g*-C₃N₄ nanosheet composite photocatalyst, which can be applied in photocatalytic reactions for CO₂ reduction and gaseous *iso*-isopropanol (IPA) oxidation under visible light irradiation, is designed and synthesized. Results demonstrate that the intimate interfacial contact and heterojunction interaction between *g*-C₃N₄ and Sb doped SnO₂ can significantly boost the photocatalytic efficiencies compared with individual *g*-C₃N₄ and Sb doped SnO₂ due to the effective separation of photo-generated charge carriers.

1. Introduction

Solar energy conversion toward chemical energy by photocatalysis is an attractive candidate solution for solving the increasing energy demand and environmental crisis due to the abundance and reproducibility of solar energy [1,2]. In search for efficient and stable photocatalysts, graphitic carbon nitride (*g*-C₃N₄) has attracted a great deal of interest in material science for the reason that g-C₃N₄ processes suitable band gap for visible light absorption, appropriate band edge positions, and good chemical and thermal stability [3,4]. *g*-C₃N₄, a typical layered structure material, has been studied in various areas such as photocatalytic pollutant degradation [5], NO removal [6], hydrogen evolution [7], oxygen evolution [8] and CO₂ reduction [9]. Nevertheless, the photocatalytic efficiency of the bulk *g*-C₃N₄ is unsatisfactory, and hampers its practical application due to high recombination rate of photogenerated electron-hole pairs. In this context, various strategies have been proposed to improve the photocatalytic performance of *g*-C₃N₄, among which the introduction of oxygen atoms and the construction of porous structure in *g*-C₃N₄ have been demonstrated to be powerful methods in achieving high photocatalytic activities [10].

However, g-C₃N₄ material alone is hardly capable for maximizing

the charge-carrier separation due to the barrier caused by exciton binding energy of semiconductors which causes disadvantages for photocatalytic reactions. Thus fabricating photocatalysts with heterojunction structures have been intensively pursued, since the efficient charge separation can be obtained by coupling two semiconductor structures with the matched energy levels, leading to the improved photocatalytic activity and efficiency. Several visible-light-driven *g*-C₃N₄/semiconductor composite photocatalysts, such as *g*-C₃N₄/NaNbO₃ [11], *g*-C₃N₄/BiPO₄ [12], *g*-C₃N₄/Ag₃PO₄ [13], *g*-C₃N₄/ZnO [14], *g*-C₃N₄/Ca₂Nb₂TaO₁₀ [15], *g*-C₃N₄/N-doped hollow-TiO₂ [16], *g*-C₃N₄/Co(OH)₂ [17], *g*-C₃N₄/Ni₂P [18], have been proved to be valuable candidates to overcome the limitation of a single *g*-C₃N₄ photocatalyst design. But regretfully, a practically viable *g*-C₃N₄ based composite photocatalyst with sufficient efficiency and high stability is yet to be demonstrated so far. Therefore it is highly desirable to develop new highly efficient and robust *g*-C₃N₄ based composite photocatalysts. For this purpose, it is significant to find a semiconductor with tunable energy band structure and energy level matching with *g*-C₃N₄.

As a traditional semiconductor material, tin oxide (SnO₂) is a better electron acceptor than TiO₂ and ZnO [19]. SnO₂ has also been reported [20–22] to possess a suitable band gap position compared to *g*-C₃N₄,

* Corresponding author at: School of Materials Science and Engineering, Shaanxi University of Science and Technology, Weiyang, Xi'an, Shaanxi 710021, PR China.
** Corresponding author at: International Center for Materials Nanoarchitectomics (WPI-MANA), National Institute for Materials Science (NIMS), 1-1 Namiki, Tsukuba, Ibaraki 305-0044, Japan.
E-mail addresses: huangjfsust@126.com, huangjf@sust.edu.cn (J. Huang), jinhua.ye@nims.go.jp (J. Ye).

which enables composite g-C_3N_4/SnO_2 to form an effective heterojunction with merits of increased separation efficiency of photo-generated electron-hole pairs at interfaces for visible light driven catalytic activity. Most importantly the band potential of the obtained g-C_3N_4/SnO_2 meets the requirement of photocatalytic CO_2 reduction that the conduction band (CB) should be negative than redox potential of CO_2/CO (-0.53 V vs. NHE, pH 7) and CO_2/CH_4 (-0.24 V vs. NHE, pH 7), respectively [23]. Further exploring the modified composite to improve the photocatalytic efficiency is necessary but far from enough. Chemical substitutional doping has been proposed as an effective way to modify SnO_2, and many doped SnO_2 materials have been successfully achieved, such as I doped SnO_2 [24], F doped SnO_2 [25], Au doped SnO_2 [26], Ti doped SnO_2 [27], and Sb doped SnO_2 [28]. Doping Sb can not only offer a convenient way to enhance the conductivity of SnO_2 due to the tailoring of the resistivity, the carrier concentrations and mobility [29], but also increase the visible light absorption of SnO_2 [22], which could be beneficial for photocatalysis.

With regard to the discussion above, we for the first time designed a novel composite photocatalyst constructed by porous g-C_3N_4 nanosheets (PCNNS) and Sb doped SnO_2 nanoparticles (SSOP). Heterojunction structure between the SSOP and PCNNS dramatically enhanced the photocatalytic activities for both the photo-reduction of CO_2 and photo-oxidation of gaseous isopropanol (IPA) due to the effective separation of electron-hole pairs. The PCNNS/SSOP composite exhibited the optimal CO_2-reduction rate of 4.49 μmol g^{-1} h^{-1} for CO evolution (21.38 times higher than BCN and 12.83 times higher than SSOP) and 0.60 μmol g^{-1} h^{-1} for CH_4 evolution (3.75 times higher than SSOP). And also the PCNNS/SSOP composite exhibited the optimal IPA oxidation rate of 565.61 ppm h^{-1} for acetone evolution (9.12 times higher than BCN and 49.61 times higher than SSOP).

2. Experimental section

2.1. Materials

Melamine, $SnCl_4$·$2H_2O$, $SbCl_3$·$2H_2O$ and aqua ammonia were purchased from Wako Co. All reagents were analytical grade and used without further purification. Deionized water (18.2 MΩ) used throughout all experiments was produced using a Millipore Direct-Q System.

2.2. Synthesis of the bulk g-C_3N_4 (BCN) and the porous g-C_3N_4 nanosheet (PCNNS)

The BCN was prepared by heating melamine at 550 °C in nitrogen for 4 h at 5 °C/min in a vacuum tube furnace. And the PCNNS was prepared by heating the BCN at 530 °C in air for 2 h at 5 °C/min in an electric meffle furnace.

2.3. Synthesis of the non-doped SnO_2 particles (NSOP) and the Sb doped SnO_2 particles (SSOP)

The NSOP and SSOP were prepared using the hydrothermal method. Firstly, 0.01 mol of $SnCl_4$·$2H_2O$ with a certain amount (0 at% Sb for NSOP and 0.7 at% Sb for SSOP) of $SbCl_3$·$2H_2O$ were dissolved in 10 mL ethanol under magnetic stirring to obtain a transparent solution. Then 40 mL deionized water was added into the solution under magnetic stirring. After that aqua ammonia was dropwise used to adjust the pH value to 10 under the continuous magnetic stirring. After that, the precursor was transformed into a Teflon autoclave with a capacity of 100 mL, and then kept at 160 °C for 12 h. After being cooled to room temperature, the powder was separated by high-speed centrifugation, washed with distilled water for several times and dried under vacuum.

2.4. Synthesis of the PCNNS/SSOP

Firstly, the PCNNS powder was evenly mixed with a certain amount of SSOP powder (1, 3, 5, 7 and 9 wt%) in ethanol under magnetic stirring for 2 h. Then the mixed powder in ethanol was dried at 40 °C under magnetic stirring. After that the dried mixed powder was heated at 400 °C in nitrogen for 2 h at 4 °C/min in a vacuum tube furnace.

2.5. Preparation of the PCNNS/SSOP photoanodes

Clean ITO glass was first obtained by sequentially washing with acetone, distilled water, and ethanol in an ultrasonic cleaner for 30 min. Then, 1.0 mg photocatalyst was well dispersed in ethanol containing nafion and stayed in an ultrasonic cleaner for 30 min. Subsequently, the suspension was doped onto 1×1 cm^2 ITO glass uniformly. After drying overnight in an oven, the electrodes were sintered at 200 °C in N_2 for 2 h to improve adhesion. The loading mass is about 1 mg/cm^2.

2.6. Characterization

Morphology of the samples was characterized by a field emission scanning electron microscope (SEM, S4800, Hitachi Co., Japan). TEM and HRTEM images were taken on a transmission electron microscope (TEM, 2100F, JEOL Co., Japan). The thickness of the samples was measured by atomic force microscopy (AFM) (Nanocute H, Japan). BET specific surface area and N_2 adsorption-desorption isotherms of samples were measured at 77 K using a surface area analyzer (BEL Japan INC., Japan). Crystal structure of the samples was determined by an X-ray diffractometer (XRD, D/max-2200, Rigaku) with Cu Kα radiation (λ = 0.15418 nm). Fourier transform infrared spectra (FT-IR) were recorded using an FT-IR spectrometer (Thermoscientific Nicolet 4700). Compositions, chemical state and valence band position of the samples were recorded on an X-ray photoelectron spectroscopy (XPS, PHI Quantera SXM, ULVAC-PHI Inc., Japan). UV–vis diffuse reflectance spectra (DRS) were performed with an UV–vis spectrophotometer (Shimadzu, UV-2600) equipped with an integrating sphere diffuse reflectance accessory. The photoluminescence (PL) spectra of samples were recorded on spectrofluorometer (JASCO FP-6500). Time-resolved fluorescence (TRF) spectra of samples were detected by a fluorescence spectrofluorometer (Quantaurus-Tau, C11367, HAMAMATSU) under the 365 nm laser excitation at room temperature. Mott-Schottky plots, photocurrent response and electrochemistry impedance spectroscopy (EIS) measurements were performed with a CHI electrochemical analyser (ALS/CH model 650A) using a standard three-electrode mode with 0.5 M Na_2SO_4 (pH 6.8) solution as the electrolyte, Ag/AgCl (saturated KCl) as the reference electrode and a Pt sheet as the counter electrode. The cleaned indium tin oxide (ITO) deposited with samples were fabricated as photoanodes.

2.7. Photocatalytic activities

To evaluate the photocatalytic activities of as-synthesized samples, the photocatalytic CO_2 reduction and the photocatalytic gaseous isopropanol (IPA) oxidation were chosen as the probe reactions.

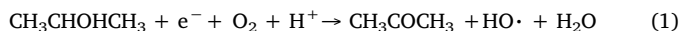#### 2.7.1. Photocatalytic CO_2 reduction activity

The photocatalytic CO_2 reduction activity of all samples were carried out in a batch-type reaction system with a total volume of about 330 mL. The setup of the photocatalytic system is illustrated in Supplementary Fig. S8. The sample was uniformly dispersed on a porous quartzose film in the reaction cell, and 5 mL of solution (MeCN/TEOA = 4:1) was injected into the cell. After complete evacuation of the reaction system (no O_2 or N_2 could be detected), 80 kPa of pure CO_2 gas was injected into the airtight system. A 300 W xenon arc lamp with a UV-cut filter, to remove light with wavelengths lower than 420 nm,

and a cooling water filter ($\lambda \geq 420$ nm) was used as the light source. In the measurements, 30 mg powder samples were used (keeping the sample at the same weight for each measurement). The gas products were measured using gas chromatography (GC-14B, Shimadzu Co., Japan).
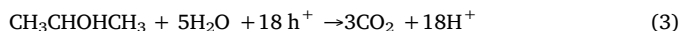
2.7.2. Photocatalytic IPA oxidation activity

For the photocatalytic oxidation of IPA, a 300 W xenon arc lamp with a UV-cut filter, to remove light with wavelengths lower than 420 nm, and a cooling water filter ($\lambda \geq 420$ nm) was used as the light source. The reactor volume was 500 mL and it was equipped with a Pyrex-glass lid as a window. The setup of the photocatalytic system is illustrated in Supplementary Fig. S10. 200 mg of the sample was spread uniformly on an 8.5 cm^2 plate which was placed in the bottom of the reactor. Then the reactor was pretreated by artificial air [$V_{(N2)}$: $V_{(O2)} = 4:1$] for 10 min to remove adsorbed gaseous impurities. A certain amount of the gaseous IPA was injected into the reactor. Before irradiation, the reactor was kept in the dark until ensuring an adsorption-desorption equilibrium of gaseous reactants on the sample. The concentrations of acetone and CO_2 were detected on a gas chromatograph (GC-14B; Shimadzu Corp., Japan) with an FID detector (Details: Porapak Q and PEG1000 column; temperatures-injection port, 120 °C; column, 60 °C; detection, 200 °C; maximum error about 7%). The IPA photodegradation undergoes two kinds of typical reaction processes as below [30,31]:

one-photon reaction:

$$CH_3CHOHCH_3 + e^- + O_2 + H^+ \rightarrow CH_3COCH_3 + HO\cdot + H_2O \quad (1)$$

or $$CH_3CHOHCH_3 + h^+ \rightarrow CH_3COCH_3 + 2H^+ + e^- \quad (2)$$

multiphoton reaction:

$$CH_3CHOHCH_3 + 5H_2O + 18h^+ \rightarrow 3CO_2 + 18H^+ \quad (3)$$

3. Results and discussion

3.1. Morphology

The formation of PCNNS/SSOP hybrid structure involved a three step process, as shown in Fig. 1 and Supplementary Fig. S1. Firstly, PCNNS were obtained by a thermal exfoliation route from bulk g-C_3N_4 (BCN) in air. The formation of abundant pores in the PCNNS is caused by the oxidation to some O-containing species which has been determined by X-ray photoelectron spectroscopy (XPS) (Supplementary Table S1) and previous reports [10,32]. Secondly, the SSOP were obtained from a facile hydrothermal method. The non-doped SnO_2 nanoparticles (NSOP) and SSOP can be prepared by a facile hydrothermal procedure, and the SEM image of SSOP is shown in Supplementary Fig.

Fig. 1. The schematic illustration of the synthetic process of the PCNNS/SSOP composite materials.

S2. The concentration of the Sb atom doped in the SnO_2 was determined by Inductively Coupled Plasma Atomic Emission Spectroscopy (ICP-AES) result, which was measured to be 0.39 at% (Supplementary Table S2). Thirdly, the as-prepared PCNNS and SSOP mixture were sintered in nitrogen atmosphere through a thermally combination process to construct the composite material. The mass percentage of SSOP in the hybrid structure can be tuned by simply increasing or decreasing the mass ratio of PCNNS and SSOP.

TEM and SEM images in Fig. 2a, b, c and Supplementary Fig. S2c show that after oxidation treatment, BCN is exfoliated into nanosheets structure with porous structure from bulk structure, and the diameter of the holes ranges from 20 nm to 500 nm. AFM image and the corresponding height image show that the thickness of PCNNS is around 1.13 nm (Fig. 2d and e).

The combination of PCNNS and SSOP in the PCNNS/SSOP heterojunction composite is verified by the high-angle annular dark-field scanning TEM (HAADF-STEM) image in Fig. 2f. The SSOP were dispersedly across the PCNNS, which forms a heterostructure with intimate interfacial contact. For more information, the selected region marked by the white lines in Fig. 2g is magnified to examine the size of the as-prepared SSOP, and it is estimated to be 2–3 nm. The selected region marked by the white lines in Fig. 2h is magnified to examine the detailed information about the interfacial structure of the composite material. As shown in HRTEM image in Fig. 2i, the well-crystallized SSOP is covered by the PCNNS. Though no lattice fringe of g-C_3N_4 is observed in Fig. 2i, its porous structure is obviously discernible. Moreover, the crystal lattice spacing of 0.33 nm alongside the interface is in accordance with the (110) facet of tetragonal cassiterite SnO_2 (JCPDS: 00-001-0657) [22,33].

As shown in Supplementary Fig. S3, the addition of 1 wt% SSOP increased the PCNNS/1 wt% SSOP specific surface area up to 40.06 m^{2}g^{-1}, which was 1.48 times higher than that of PCNNS (27.13 m^{2}g^{-1}). Increased amount of SSOP does continually increase the specific surface area of the composite and reached the maximum (56.11 m^{2}g^{-1}) when adding content is 9 wt%. It is worth mentioning that the formed hybrid structure could effectively improve the specific surface area of PCNNS due to the introduction of SSOP (Supplementary Table S3), which is beneficial to the phtocatalytic activity by providing abundant reactive sites to trap charge carriers and adsorb reactant species [34,35].

3.2. Crystal structure and chemical bonds

X-ray diffraction (XRD) patterns were employed to identify the crystallographic structure and the phase purity of the as-synthesized samples (Fig. 3a). The two main peaks located at 12.88° and 27.69° in the pure PCNNS and the five PCNNS/SSOP composite samples are assigned to the diffraction of the (100) and (002) planes of the hexagonal phase of graphitic C_3N_4 (JCPDS 87-1526), respectively [36,37]. The diffraction peaks of pure SSOP at 26.59°, 33.77°, 37.98°, 51.70° and 65.27° can be indexed as (110), (101), (200), (211) and (112) diffraction planes of the tetragonal cassiterite SnO_2 (JCPDS: 00-001-0657) [38,39], respectively. The XRD patterns of BCN and PCNNS were shown in Supplementary Fig. S4a, and the XRD patterns of non-doped SnO_2 particles (NSOP) and SSOP were presented in Supplementary Fig. S4b. It proves that the crystal structure of PCNNS is largely retained after the oxidation process. The (100) peak of the PCNNS sample exhibits slight blue shift compared with the BCN sample, corresponding to the increase in the distance of in-planar nitride pores according to Bragg equation. This feature could be interpreted as the successful doping of Sb atoms in the SSOP and the consequential disturbance of the SnO_2 structure, in agreement with previous reports. Meanwhile, the (002) peak of the PCNNS sample exhibits slight red shift compared with the BCN sample, corresponding to a decrease in the interplanar stacking distance (Supplementary Fig. S4a and Supplementary Table S4). This feature could be interpreted as the introduction of oxygen heteroatoms
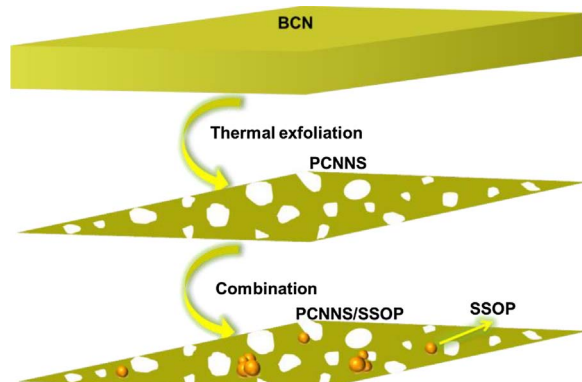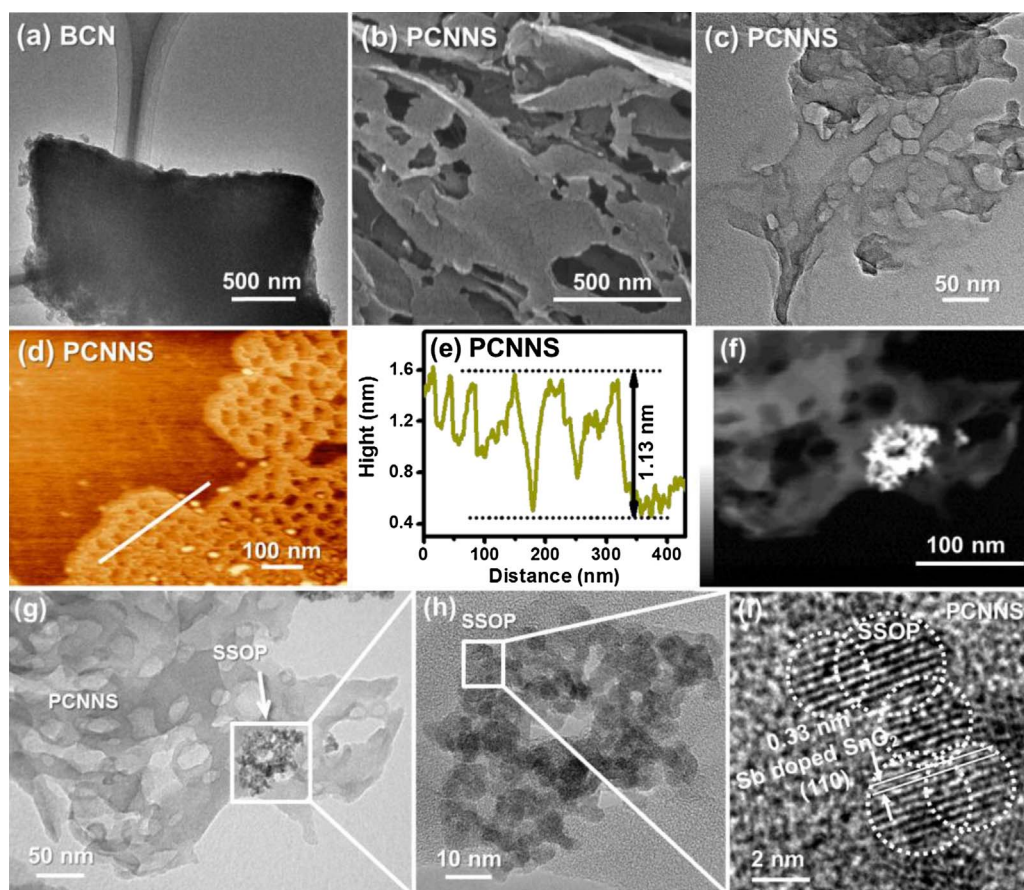
Fig. 2. (a) TEM images of the as-synthesized BCN sample; (b) SEM, (c) TEM, (d) AFM image and (e) the corresponding height images of the as-synthesized PCNNS sample, respectively; (f) the high-angle annular dark-field scanning TEM (HAADF-STEM) image of the PCNNS/5 wt% SSOP composite; TEM images of (g) PCNNS/5 wt% SSOP composite and (h) SSOP (0.39 at% Sb) in the composite; (i) HRTEM image of the SSOP in the composite.

and the consequential disturbance of graphitic structure, in agreement with previous reports [10]. The (110) peak shifting to lower angles and the corresponding increasing interplanar spacing of the as-synthesized SSOP compared with the NSOP could demonstrate the successful Sb-doping in SnO_2 (Supplementary Fig. S4b and Supplementary Table S5) [22]. The five PCNNS/SSOP composite photocatalysts show two sets of diffraction peaks of PCNNS and SSOP. No additional peaks are observed in XRD pattern of the PCNNS/SSOP composites, confirming that the composites only contain PCNNS and SSOP. After coupling SSOP on PCNNS, the PCNNS/SSOP exhibited the same crystal structure as that of the pure PCNNS sample, indicating that no obvious change took place in the crystal structure of PCNNS/SSOP. Moreover, with the increased amount of the SSOP in the composite samples, the increased intensities of (101) and (112) peaks of the SSOP sample (JCPDS: 00-001-0657) were also observed.

XRD results were further confirmed by FT-IR investigation. The

FTIR spectra of PCNNS, PCNNS/5wt%SSOP and SSOP are shown in Fig. 3b. As to PCNNS, the peak at 808 cm^{-1} is related to the s-triazine ring mode [10,13,14]. The typical absorption peaks at 1244 cm^{-1}, 1324 cm^{-1}, 1411 cm^{-1}, 1459 cm^{-1}, 1570 cm^{-1} and 1635 cm^{-1} can be correspond to the typical stretching modes of the CN heterocycles [10,32,35]. The peak at 3166 cm^{-1} is ascribed to the secondary and primary amines [10,34,40]. Moreover, for SSOP, peaks around 533 and 658 cm^{-1} observed in the spectrum is ascribed to Sn−O stretching mode [41,42]. The peak at 1450 and 1628 cm^{-1} is respectively assigned to the molecular water and hydroxyl groups on the surface of SnO_2 [43,44]. The FTIR spectra in Supplementary Fig. S5a further demonstrate that the core chemical structure of the BCN is maintained in the PCNNS. Peaks slightly shift toward higher wavenumbers (Supplementary Fig. S5b,c) indicating that the weakened interactions between the "nitrogen pots" in PCNNS compared to BCN probably caused by the partial substitution of N atoms by O atoms [10,32]. In the FTIR
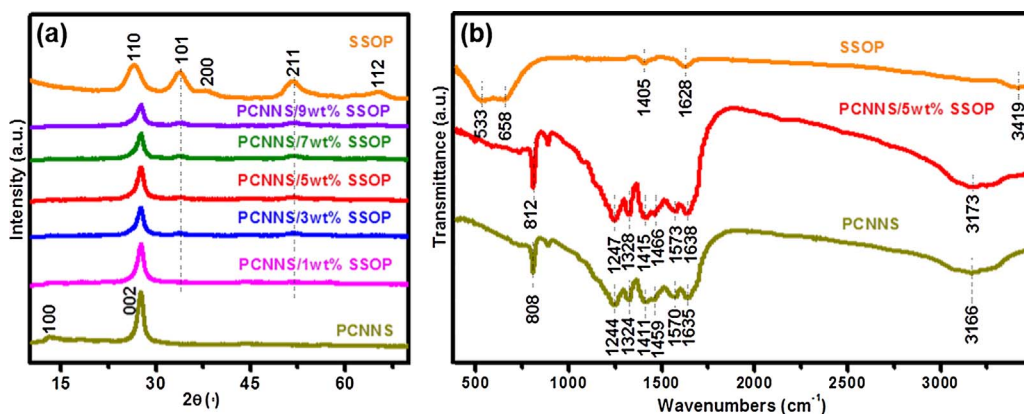

Fig. 3. (a) XRD patterns of PCNNS, PCNNS/SSOP composites with different content (1, 3, 5, 7 and 9 wt%) and SSOP samples (b) and FT-IR spectra of PCNNS, PCNNS/5 wt% SSOP composites and SSOP samples.
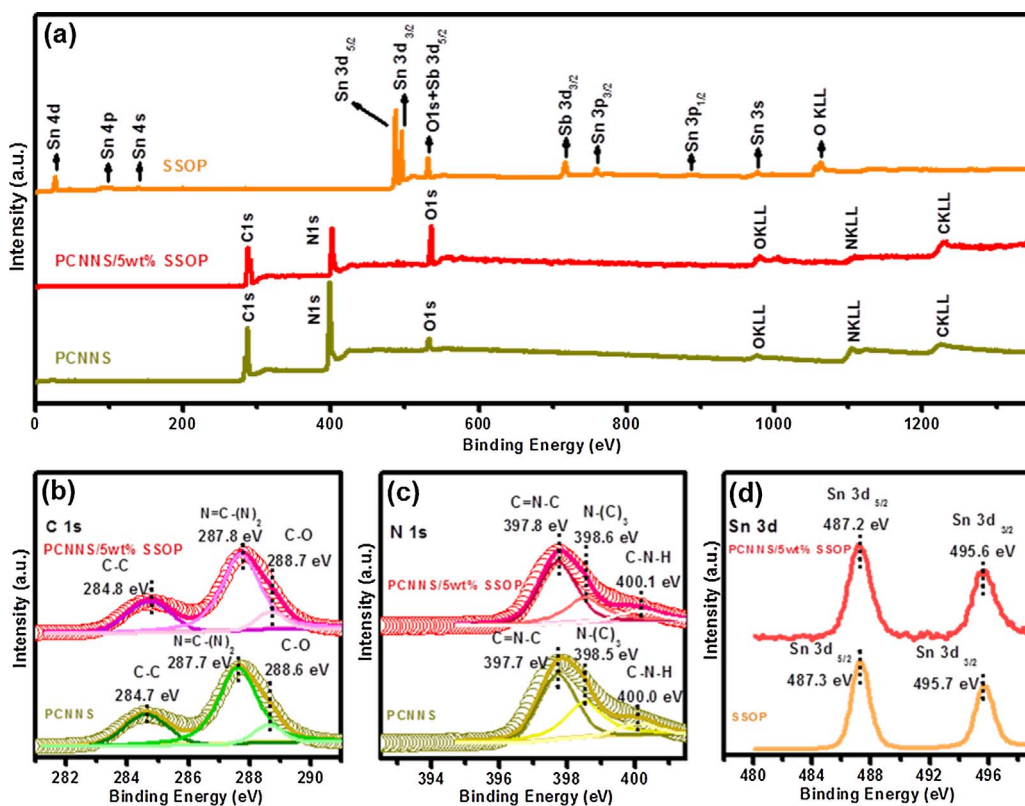
Fig. 4. (a) Wide range XPS spectra, (b) C 1 s high-resolutions, (c) N 1 s high-resolutions, (d) Sn 3d high-resolutions XPS spectra of the PCNNS, the PCNNS/5 wt% SSOP and the SSOP samples.

spectrum of PCNNS/5wt%SSOP composite, the main characteristic peaks of PCNNS can be clearly seen, while the main characteristic peaks of SSOP cannot be clearly seen due to the low content of SSOP in this composite [22]. The FTIR spectrum further reveals all the main characteristic peaks of PCNNS/5wt%SSOP moving to higher wavenumbers. The red shift of these bands indicates that there is a strong interaction between PCNNS and SSOP in the composites, which is advantageous to enhancing its visible-light photocatalytic activity due to the effective transfer of carriers between PCNNS and SSOP [14,42].

The above discussion demonstrates the formation of PCNNS/SSOP heterojunction composite. To further probe the chemical environment and chemical composition of the elements of as-prepared composite, XPS measurements were performed. The survey spectra indicate the presence of C, N, O in PCNNS, C, N, O, Sn, and Sb in the PCNNS/5 wt% SSOP composite, and Sn, O and Sb in SSOP, respectively (Fig. 4a and Supplementary Fig. S6a). To gain more insight into the chemical bonding in the composite, the high resolution XPS spectra were deconvoluted by Gaussian-Lorenzian analysis method. For C 1 s spectra, three distinct peaks at 284.8, 287.8 and 288.7 eV are attributed to C−C, N=C−$(N)_2$ and C−O, respectively for the PCNNS/5 wt% SSOP (Fig. 4b), and 284.7, 287.7 and 288.6 eV are ascribed to C−C, N=C−$(N)_2$ and C−O, respectively for PCNNS (Fig. 4b and Supplementary Fig. S6b) [10,45–47]. Thus, these results could confirm the existence of g-C_3N_4 in the composite. The O 1 s peaks of BCN and PCNNS can be deconvoluted into three components, and the peaks centred at 531.9, 532.8, and 534.1 eV are ascribed to C−O, H_2O and O_2, respectively [47] (Supplementary Fig. S6d). Meanwhile, the N 1 s peaks for the PCNNS/5 wt% SSOP and PCNNS can be deconvoluted into three peaks with binding energy at 397.8, 398.6 and 400.1 eV (Fig. 4c and Supplementary Fig. S6c) and these peaks can be ascribed to C−N=C, N−$(C)_3$ and C−N−H, respectively [46,47]. XPS survey spectra of the SSOP and NSOP confirm that Sb has been successfully doped into the SSOP (Supplementary Fig. S7a). High resolution Sn 3d spectra of the PCNNS/5 wt% SSOP, SSOP and NSOP show two peaks at 487.2 and 495.6 eV, corresponding to Sn $3d_{5/2}$ and Sn $3d_{3/2}$, respectively [48,49] (Fig. 4d

and Supplementary Fig. S7b). As shown in Supplementary Fig. S7d, the Sb $3d_{3/2}$ peaks of the SSOP and NSOP were employed to quantify the antimony content by Gaussian deconvolution into components centered at 540.0 eV for Sb^{3+} and 540.5 eV for Sb^{5+}, respectively [50,51]. The atomic ratio of Sb (III) state to Sb (V) state of SSOP and NSOP can be obtained from the deconvolution of the Sb $3d_{3/2}$ XPS peak and are presented in Supplementary Table S7. It demonstrates that Sb is successfully doped into SnO_2, which may exhibit distinct optical and photoelectrochemical properties.

It is worth noting that for the PCNNS/5 wt% SSOP, both peaks of Sn 3d shift toward lower binding energies compared to the SSOP, while N 1 s and C 1 s (mainly the peak of C−N−C coordination) shift toward higher binding energies relative to PCNNS. These shifts might result from a partial electron transfer from the electron-rich structure of PCNNS to SSOP, and this would increase the electron density of SSOP, leading to reduction of the binding energies of Sn 3d. On the other hand, the electron density of PCNNS could be decreased, leading to the enhancement of binding energies of N 1s and C 1s. All the shifts for binding energy in the XPS spectra can be attributed to the intense interaction between the closely contacted phases of SSOP and PCNNS, indicating a strong electronic interaction between PCNNS and SSOP and thus further implying that the heterojunctions with strong electronic interaction between PCNNS and SSOP have been formed in the as-synthesized composite [52,53]. The strong electronic interaction between PCNNS and SSOP in the PCNNS/SSOP composite may be beneficial to the transfer of photoinduced charges during the photocatalytic process.

3.3. UV–vis DRS spectra

The optical properties of the PCNNS/SSOP heterojunction composites were evaluated by UV–vis diffusive absorption spectroscopy. Fig. 5a shows the ultraviolet-visible diffusive absorption spectra of PCNNS and PCNNS/SSOP composites with varying content of SSOP. The absorption spectrum of PCNNS/SSOP possesses the hybrid
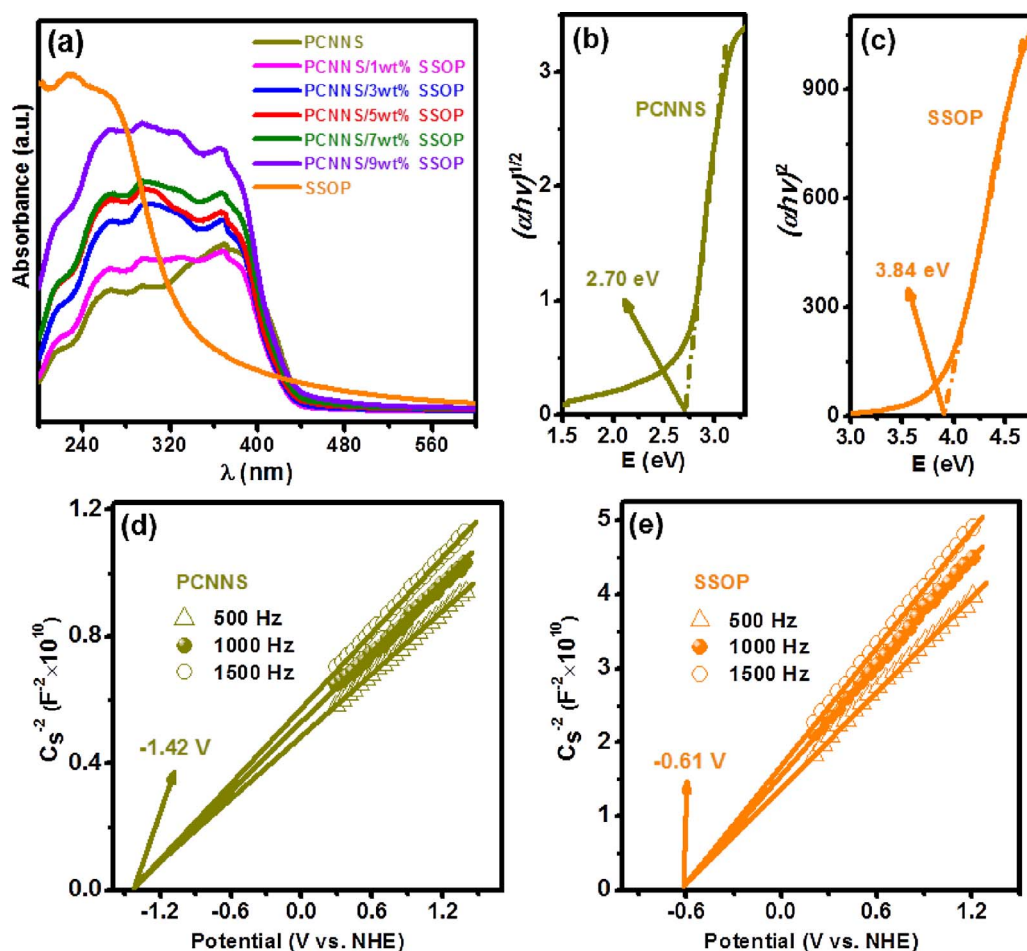
Fig. 5. (a) UV–vis diffuse reflectance spectra of the as-prepared pure PCNNS, PCNNS/SSOP composites with different SSOP content (1, 3, 5 and 9 wt%) and pure SSOP samples. The calculated bandgaps of the (b) PCNNS and (c) SSOP samples. Mott-Schottky plots at the frequencies of 500, 1000 and 1500 Hz in 0.5 M Na_2SO_4 aqueous solution of (d) PCNNS and (e) SSOP samples.

absorption features of both spectra which contribute from PCNNS and SSOP. Consequently, the enhanced adsorption in the whole light range of the PCNNS/SSOP may imply the more efficiency in exploiting the sunlight for the photocatalytic purpose.

It can be seen that the as-prepared PCNNS, PCNNS/SSOP composites with varying SSOP content (1, 3, 5, 7 and 9 wt%) absorb visible-light with wavelengths at around 450 nm, and pure SSOP can absorb visible-light with wavelengths above 500 nm (Fig. 5a). As indirect bandgap semiconductor, the band gap of PCCNS can be estimated from the UV–vis spectra to be 2.70 eV (Fig. 5b) [10]. And as a direct bandgap semiconductor, the intrinsic bandgap of SSOP can be calculated to be 3.84 eV (Fig. 5c). It should be noted that doping Sb into SnO_2 could introduce a lot of defects, which is responsible for its extended light absorption in the visible light region [22,54]. Approximate conduction band (CB) edge positions of the as-synthesized samples based on the above-measured flat-band (FB) potential in the *n*-type semiconductor can be calculated by Mott-Schottky plots [55,56], and the value is −1.42 and −0.61 V vs. NHE, pH = 7 for pure PCNNS and SSOP, respectively (Fig. 5d and e).

3.4. Photocatalytic performance

3.4.1. Photocatalytic CO_2 reduction

It is obvious that the positions of the conduction band of g-C_3N_4 are negative enough to reach the corresponding redox potential of CO_2 to produce CO and CH_4, respectively (Fig. 5d, e). To prove the superiority of PCNNS/SSOP composite in photocatalysis, the photocatalytic CO_2 reduction over PCNNS/SSOP composite was carried out by using trie-thanolamine as the electron donor in acetonitrile under atmospheric CO_2 and visible light (the experimental setup was shown in

Supplementary Fig. S8). The CO_2 photoreduction products for the samples include CO and CH_4, while there are no CH_4 detectable for pure BCN. Fig. 6a and c show the time dependent conversion yields of CO_2 into CO and CH_4, respectively, using the pure BCN, pure PCNNS, the PCNNS/SSOP composite with different amount of SSOP (1, 3, 5, 7 and 9 wt%) and the pure SSOP samples as photocatalysts under visible light. The pure SSOP also shows the photocatalytic performance for CO_2 reduction under visible light despite its large bandgap, which is due to the presence of defects [22,50]. Pure non-doped SnO_2 does not show any photocatalytic performance for CO_2 reduction under visible light, because it cannot absorb visible light (Supplementary Fig. S9). With the increase of the SSOP content in the composites, the yields of CO and CH_4 increase firstly till the SSOP content reaches 5 wt%, then decrease with adding more SSOP. The yields of CO and CH_4 increase almost linearly with the irradiation time and it is obvious that PCNNS/5 wt% SSOP displays sustainable CO and CH_4 evolution activity and it attained yields of 22.47 µmol g_{cat}^{-1} and 2.98 µmol g_{cat}^{-1}, respectively under visible light for 5 h, which is much higher than that of BCN (1.07 µmol g_{cat}^{-1} for CO evolution, and 0 µmol g_{cat}^{-1} for CH_4 evolution), PCNNS (4.66 µmol g_{cat}^{-1} for CO evolution, and 0.53 µmol g_{cat}^{-1} for CH_4 evolution) and SSOP (1.76 µmol g_{cat}^{-1} for CO evolution, and 0.78 µmol g_{cat}^{-1} for CH_4 evolution) as shown in Fig. 6b, respectively. And the corresponding yield rates of CO and CH_4 from photocatalytic CO_2 reduction over PCNNS/5 wt% SSOP (4.49 µmol g_{cat}^{-1} h^{-1} CO evolution, 0.60 µmol g_{cat}^{-1} h^{-1} CH_4 evolution) under visible light for 5 h is much higher than that of BCN (0.21 µmol g_{cat}^{-1} h^{-1} CO evolution, 0 µmol g_{cat}^{-1} h^{-1} CH_4 evolution), PCNNS (0.93 µmol g_{cat}^{-1} h^{-1} CO evolution, 0.11 µmol g_{cat}^{-1} h^{-1} CH_4 evolution) and SSOP (0.35 µmol g_{cat}^{-1} h^{-1} CO evolution, 0.16 µmol g_{cat}^{-1} h^{-1} CH_4 evolution), respectively. Control experiments showed that no detectable CO
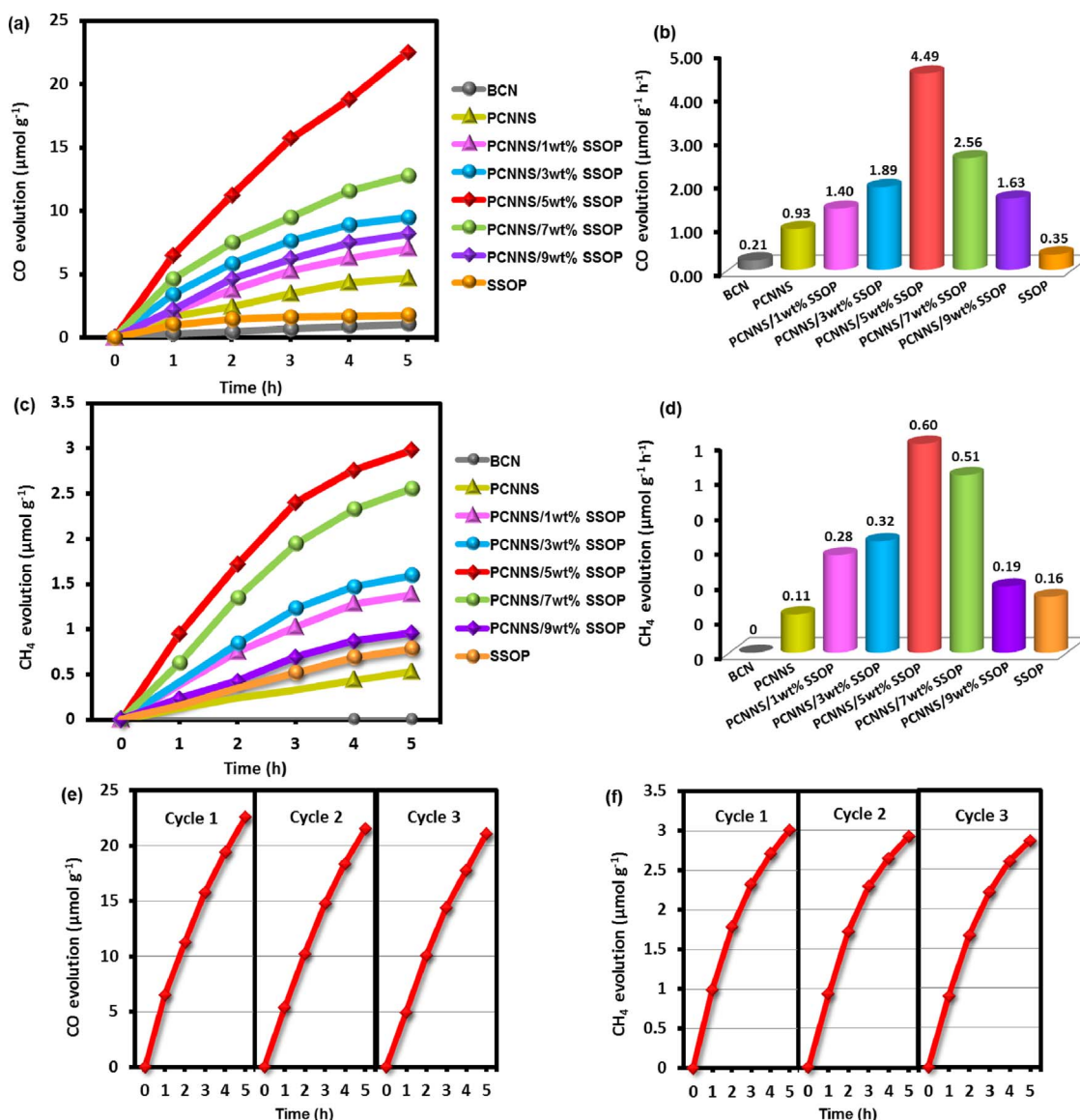
Fig. 6. (a) Time course of the photocatalytic CO evolution, (b) comparison of the corresponding CO evolution amount, (c) time course of the photocatalytic CH_4 evolution, (d) comparison of the corresponding CH_4 evolution amount over the BCN, the PCNNS, the PCNNS/SSOP samples with varying content (1, 3, 5, 7 and 9 wt%) of SSOP and the pure SSOP, (e) photocatalytic cycle activity for CO evolution over the PCNNS/5wt%SSOP sample and (f) photocatalytic cycle activity for CH_4 evolution over the PCNNS/5wt%SSOP sample, respectively, from photocatalytic CO_2 reduction.

and CH_4 were found in the reaction system in the absence of photocatalysts or light illumination, demonstrating that the CO and CH_4 evolution by the proposed samples was induced by photocatalytic pathways. The generation of the products may be explained by the rapid carriers separation caused by the formation of heterojunctions between PCNNS and SSOP in the composites. With the increase of the SSOP content, the PCNNS/SSOP heterojunction facilitates the separation of the photo-induced electrons and holes, resulting in the improvement of the photocatalytic yield rates of CO and CH_4. However, when the SSOP content is over 5 wt% in the PCNNS/SSOP composite, the excessive SSOP with excessive surface defects may act as the recombination centers of photogenerated electrons and holes thus leading to forming obstruction for the photocatalytic reaction for CO_2 reduction [22,50]. Thus, the drop of the productivity should be ascribed to the decreasing the separation efficiency of electron-hole pairs. The photocatalytic CO_2 reduction stability of the PCNNS/5 wt% SSOP composite is evaluated by the cycle test in Fig. 6e and f, and the results show that this PCNNS/5 wt% SSOP composite possesses good photocatalytic CO_2 reduction stability.

3.4.2. Photocatalytic IPA oxidation

The photocatalytic performance of the samples was further investigated by the oxidation of gaseous IPA under visible light irradiation (the experimental setup was shown in Supplementary Fig. S10). The dominant product from this IPA photocatalytic oxidation was acetone, and trace amount of CO_2 production was also observed. As shown in Fig. 7a and b, pure BCN, pure PCNNS, the PCNNS/SSOP composite with different amount of SSOP (1, 3, 5, 7, 9 wt%) and the pure SSOP samples present obviously different acetone evolution amount (62.03, 276.77, 409.47, 470.26, 565.61, 351.51, 305.19 and 11.4 ppm h^{-1} for acetone evolution, respectively) under visible light for 4 h. It is interesting to find that the pure SSOP sample also shows photocatalytic activity under visible light in spite of its large bandgap (3.84 eV), as shown in Fig. 5c. The presence of defect levels is responsible for its visible light absorption and photocatalytic activity, as demonstrated in the previous discussion [22,50]. Pure non-doped SnO_2 does not show any photocatalytic performance for IPA oxidation under visible light, because it cannot absorb visible light (Supplementary Fig. S9). After thermally oxidation, the PCNNS shows obviously enhanced
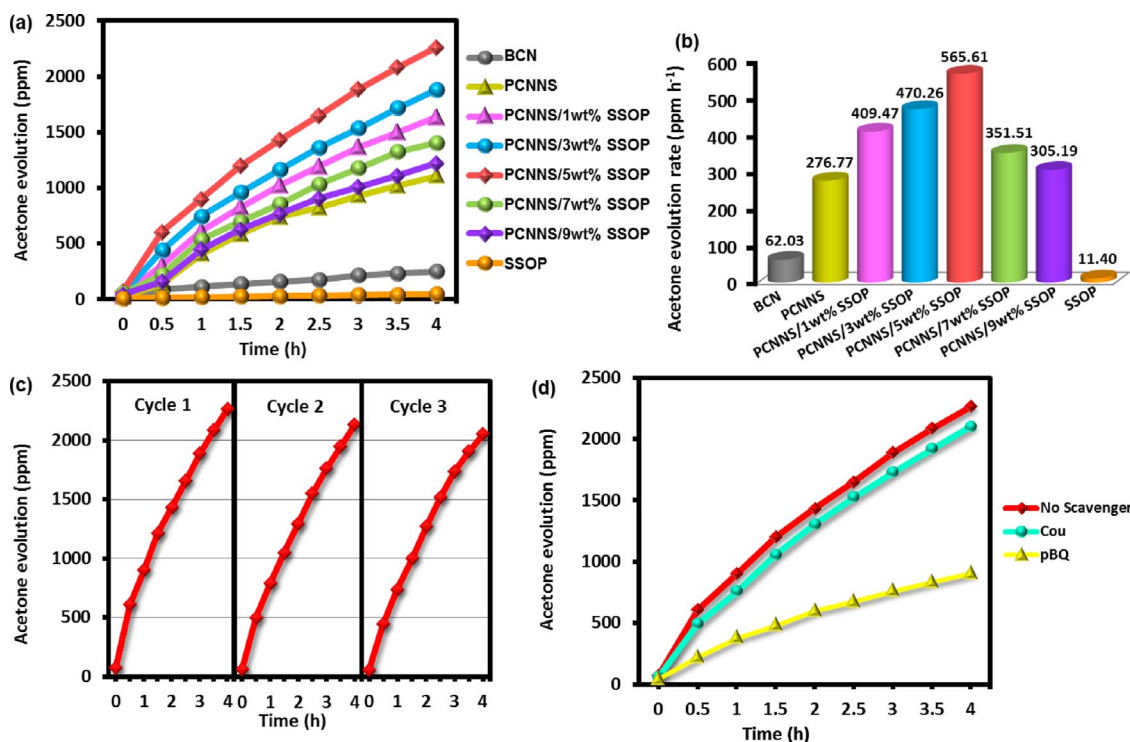
Fig. 7. (a) Time course of the photocatalytic acetone evolution, (b) comparison of the corresponding acetone evolution amount over the pure BCN, the pure PCNNS, the PCNNS/SSOP with varying SSOP content (1, 3, 5, 7 and 9 wt%) and the pure SSOP samples, (c) photocatalytic cycle activity for acetone evolution over the PCNNS/5wt%SSOP sample and (d) photocatalytic activity for acetone evolution over the PCNNS/5wt%SSOP sample with different reactive-species scavengers, respectively, from photocatalytic IPA oxidation.

photocatalytic oxidation of IPA than BCN. Then adding 1 wt% SSOP significantly enhances the photocatalytic IPA oxidation activity of the PCNNS/1 wt% SSOP compared to BCN and PCNNS. The photocatalytic IPA oxidation of PCNNS/SSOP composite presents to be raised with the increasing SSOP content till the activity reaches the maximum value when SSOP content is 5 wt%. Then with the continually increased SSOP content, the photocatalytic IPA oxidation activity drops. The PCNNS/ 5 wt% SSOP composite exhibits superior photocatalytic IPA oxidation activity (565.61 ppm h^{-1} for acetone evolution) compared with that of other composite samples under visible light for 4 h, which is much higher than that of BCN (62.03 ppm h^{-1} for acetone evolution), PCNNS (276.77 ppm h^{-1} for acetone evolution) and SSOP (11.4 ppm h^{-1} for acetone evolution). Control experiments showed that the acetone produced from IPA in the absence of any catalysts or light irradiation could be neglected, respectively, which demonstrated that the acetone was produced from the samples through a photocatalytic pathway. Thus, it may be reasonably deduced that the formation of heterojunctions between the interfacial phases are responsible for the enhanced photocatalytic activity of the synthesized composites. But excessive SSOP displays no contribution to the improvement of the photocatalytic activity of the PCNNS/SSOP composite. The stability of photocatalytic IPA oxidation over PCNNS/5wt%SSOP composite was studied by re-using the photocatalyst for three cycles, which shows fairly good photocatalytic stability (Fig. 7c). The photocatalytic CO$_2$ reduction and photocatalytic IPA oxidation experiments indeed demonstrate the superiority and promising prospect of PCNNS/SSOP in artificial photosynthesis. Reported by previous work, upon light irradiation, the photogenerated electrons of photocatalyst can combine with a molecule of O$_2$ to produce the $\cdot$O$_2^-$ radical, and then the $\cdot$O$_2^-$ oxidizes IPA to become acetone; or the photoexcited holes directly oxidize IPA into acetone [30,31]. In this case, the photooxidization of IPA to acetone is a one-photon process.

To investigate the reactive oxygen-related species in the photooxidation process, we further studied the active species of PCNNS/5wt %SSOP composite for gaseous photocatalytic IPA oxidation by

introducing scavengers. The coumarin (Cou), *p*-benzoquinone (pBQ) were used as the scavengers for $\cdot$OH and $\cdot$O$_2^-$, respectively [57]. For the PCNNS/5wt%SSOP composite sample, only the electron-induced $\cdot$O$_2^-$ radical participates in the photocatalytic IPA oxidation, because only the pBQ introduction obviously suppresses the photoactivity (Fig. 7d).

3.5. Photocatalytic mechanism investigation

In order to prove that the rapid charge separation has been obtained in the designed composite, PL spectroscopy measurements for PCNNS, PCNNS/SSOP heterojunction composite and the pure SSOP samples were investigated. The pure PCNNS exhibits a strong emission in the range of 400 ~ 600 nm, which corresponds to the carrier recombination [46] (Fig. 8a). When the SSOP was added, the PL emission intensity decreases markedly, which suggests that the photoinduced charge could be efficiently separated when the heterojunction was formed between PCNNS and SSOP, and this further confirmed the photocatalytic mechanism proposed. The PL emission intensity followed the order: pure BCN > pure PCNNS > PCNNS/5wt%SSOP, indicating that the electron transfer efficiency of the samples followed the order: PCNNS/5wt %SSOP > pure PCNNS > pure BCN, which may result in enhanced photocatalytic activity in this PCNNS/SSOP composite.

Further insight into the electron transfer behavior was gained by the time-resolved PL decays (Fig. 8b). The decay curves could be fitted well with tri-expontial functions and the calculated average lifetime values are presented in Fig. 8b. It can be seen that PCNNS/5wt%SSOP (8.16 ns) exhibits a longer average lifetime than pure BCN (7.28 ns) and pure PCNNS (7.87 ns), indicating that the recombination of photoexcited electron-hole pairs have been inhibited in this composite.

The photoelectrochemical (PEC) performance is widely considered to be efficient evidence for demonstrating the electron-hole pair separation and transfer in the composite photocatalysts [55]. Accordingly, the transient photocurrent-time (I-t) curves and electrochemical impedance spectroscopy (EIS) of the BCN, pure PCNNS and PCNNS/
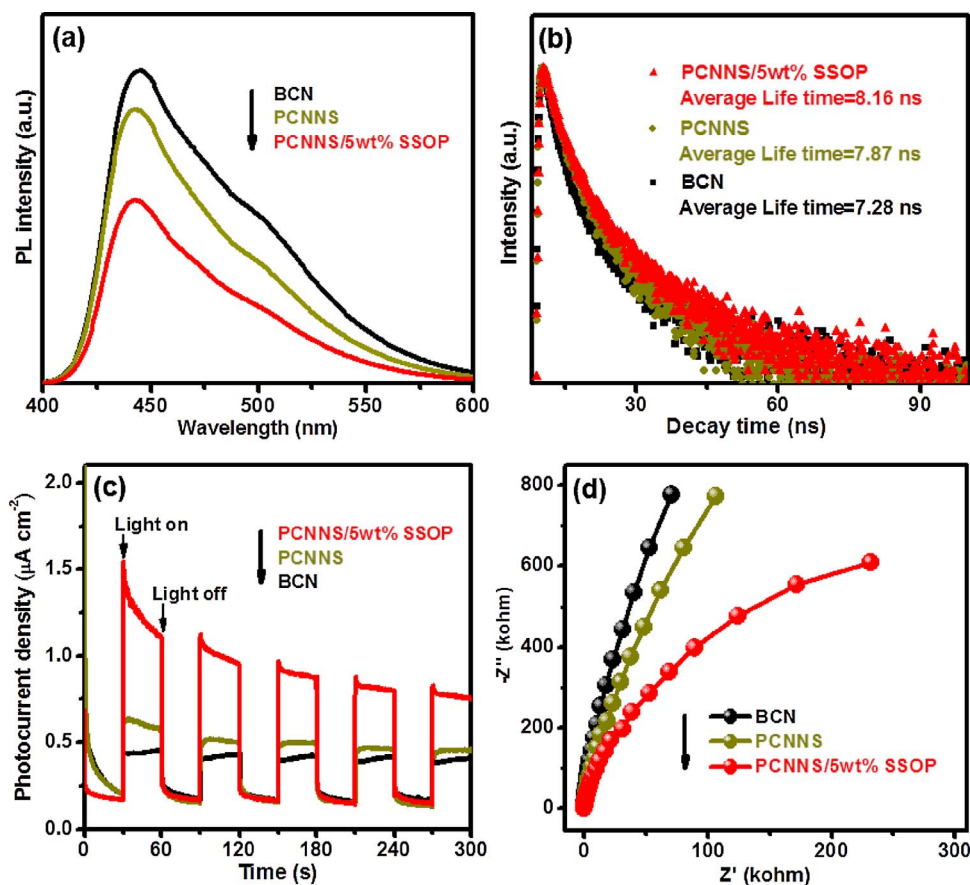
Fig. 8. (a) Photoluminescence (PL) spectra, (b) time-resolved transient PL decays spectra, (c) photocurrent-time dependence curves under visible light irradiation and (d) electrochemistry impedance spectroscopy (EIS) curves of the pure BCN, the pure PCNNS and the PCNNS/5wt%SSOP composite samples.
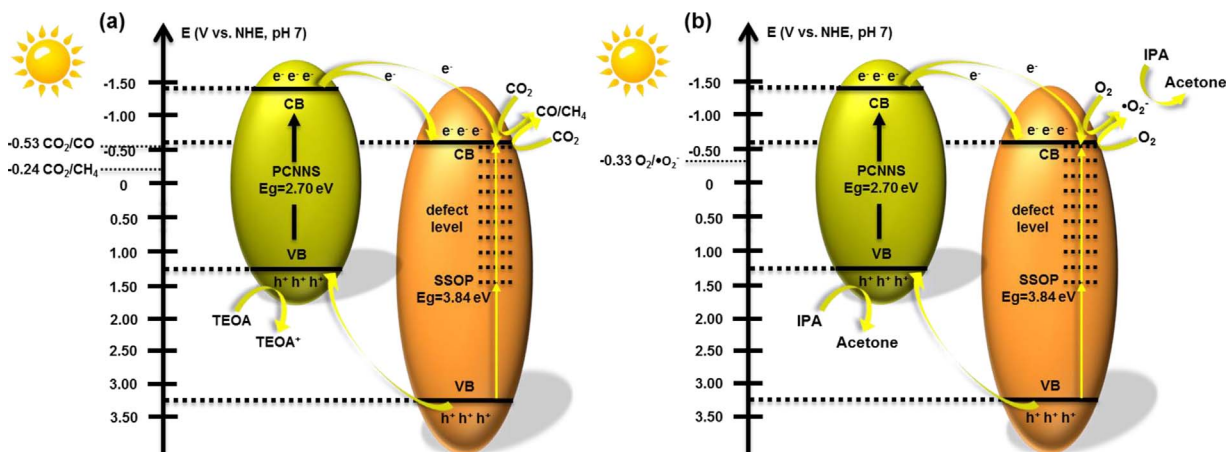

Fig. 9. Schematic energy level diagram of the pure PCNNS and pure SSOP samples, and the electron transfer dynamics involved in photocatalytic (a) CO_2 reduction and (b) photocatalytic IPA oxidation.

Table 1
Physicochemical characterization of the BCN, the PCNNS, the PCNNS/SSOP composite with varying SSOP content (1, 3, 5, 7 and 9 wt%) and the pure SSOP samples.

Sample	Sb-SnO$_2$ content (wt%)	S$_{BET}$ (m^2 g^{-1})	CO$_2$ reduction		IPA oxidation
			CO evolution (μmol g^{-1} h^{-1})	CH$_4$ evolution (μmol g^{-1} h^{-1})	Acetone evolution (ppm h^{-1})
BCN	0	9.56	0.21	0	67.03
PCNNS	0	27.13	0.93	0.11	276.77
PCNNS/1wt%SSOP	1	40.06	1.40	0.28	409.47
PCNNS/3wt%SSOP	3	43.19	1.89	0.32	470.26
PCNNS/5wt%SSOP	5	46.87	4.49	0.60	565.61
PCNNS/7wt%SSOP	7	49.55	2.56	0.51	351.51
PCNNS/9wt%SSOP	9	56.11	1.63	0.19	305.19
SSOP	100	156.00	0.35	0.16	11.40

SSOP heterojunction composite were further measured. Fig. 8c shows a comparison of the I-t curves for these samples with typical on-off cycles of intermittent visible light irradiation. Notably, the photocurrent value of PCNNS/SSOP is obviously higher than the pure BCN and pure PCNNS, which can be ascribed to the existence of interfaces between PCNNS and SSOP, where photogenerated electrons and holes could be efficiently separated in space and the photoinduced carrier recombination could be suppressed [58]. As a result, the improved transfer efficiency of charge carriers could lead to the enhanced photocatalytic activity. From the EIS spectra in Fig. 8d, the arc radius of the EIS Nyquist plot of the PCNNS/SSOP is found to be smaller than that of the pure BCN and the pure PCNNS. Given that the arc radius on the EIS spectra reflect the reaction rate at the surface of an electrode [56], the data in the EIS Nyquist plots suggest the more effective separation of photo-generated electron-hole pairs and a faster interfacial charge transfer on PCNNS/SSOP under this condition. This result is consistent with the PL and PEC analyses, and clearly indicates that the introduction of SSOP into PCNNS can effectively enhance the separation efficiency of photogenerated electron-hole pairs.

With the combination of calculated bandgaps and CB positions, schematic energy level diagrams of the PCNNS and the SSOP samples can be proposed in Fig. 9. The band potentials of the obtained PCNNS and SSOP both meet the requirement of photocatalytic CO_2 reduction, and their CB positions are more negative than the redox potential of CO_2/CO (-0.53 V vs. NHE, pH 7) and CO_2/CH_4 (-0.24 V vs. NHE, pH 7) [23], respectively. It means that the photocatalytic CO_2 reduction can be expected in the PCNNS/SSOP composite. On the basis of the above discussion, a tentative mechanism for the photocatalytic CO_2 reduction over the PCNNS/SSOP composite is proposed (Fig. 9a). Upon visible light irradiation electrons are excited from the valence band of PCNNS to its corresponding conduction band [59]. Those photogenerated electrons migrate to the surface of PCNNS and then transfer to the CB and the defects levels of SSOP across the interface between PCNNS and SSOP, which leads to the spatial separation of photogenerated charges. The electrons on the CB or the defect levels of SSOP above the redox potential of CO_2/CO (-0.53 V vs. NHE, pH 7) and CO_2/CH_4 (-0.24 V vs. NHE, pH 7) [23] transferred from PCNNS can reduce CO_2 to produce CO and CH_4, and the holes that remained within the valence band of PCNNS are consumed by TEOA, which acts as an electron donor. Additionally, the SSOP can also absorb photons of visible light to excite the electrons from its VBM to surface defects levels and then promote the electrons to the higher levels (above the CO_2 reduction potential) to induce the reduction of CO_2 to produce CO and CH_4. Meanwhile, photo-induced holes remained on the VBM of SSOP can migrate to PCNNS, and are consumed by TEOA.

The photocatalytic mechanism for the photocatalytic IPA oxidation over the PCNNS/SSOP composite is proposed, as shown in Fig. 9b. Upon visible light irradiation, the photogenerated electrons from PCNNS transfer to the CB and the defects levels of SSOP across the interface between PCNNS and SSOP. The electrons on the CB or the defect levels of SSOP above the redox potential of $O_2/\cdot O_2^-$ (-0.33 V vs. NHE, pH 7) can produce $\cdot O_2^-$ radicals [60], and then oxidize IPA to acetone. The holes that remained within the valence band of PCNNS can oxidize IPA. Additionally, the SSOP can also absorb photons under visible light to excite the electrons from its VBM to surface defects levels and then promote the electrons to the higher levels (above the redox potential of $O_2/\cdot O_2^-$) to induce the production of $\cdot O_2^-$ radicals to oxidize IPA. Meanwhile, photo-induced holes remained on the VBM of SSOP can migrate to PCNNS and then also oxidize IPA to acetone.

To summarize, all the information was collected in Table 1. From Table 1, it could be seen that compared with BCN, PCNNS with porous structures shows enhanced photocatalytic CO_2 reduction and IPA oxidation activities due to the increased the specific surface area [10]. All the PCNNS/SSOP composites presented better photocatalytic CO_2 reduction and IPA oxidation activities than pure BCN, PCNNS and SSOP because of the formation of heterojunction interaction between PCNNS

and SSOP. And the photocatalytic CO_2 reduction and IPA oxidation activities of PCNNS/SSOP raised with the increased SSOP content, then reached its maximum when SSOP content was 5 wt%. With excessive SSOP, the drop of the activities should be ascribed to the decreased separation efficiency of electron-hole pairs induced by the excessive surface defects which acted as the recombination centers of photogenerated electrons and holes, leading to the formation of obstructions for the photocatalytic reactions [22,49].

4. Conclusions

In conclusion, we presented a novel photocatalyst for CO_2 photoreduction and IPA photo-oxidation with effectively intimate porous *g*-C_3N_4 nanosheets/Sb doped SnO_2 particles heterostructure composite. Under an optimal experimental condition, the PCNNS/5wt%SSOP composite photocatalyst exhibits the optimal photocatalytic performance owing to the formation of heterojunction between the porous *g*-C_3N_4 nanosheets and the Sb doped SnO_2 particles. The mechanism was inferred and further evidenced that it is the PCNNS/SSOP heterojunction composite promoting the separation of the photo-induced carriers enhanced the photocatalytic CO_2 reduction and IPA oxidation. This study on the direct solid-state porous *g*-C_3N_4 nanosheets/Sb doped SnO_2 particles not only may provide useful information for further development of novel heterojunction photocatalytic systems based on composite photocatalyst, but also could be significant in meeting the demands of environmental domains.

Acknowledgements

Appendix A. Supplementary data

Supplementary data associated with this article can be found, in the online version, at http://dx.doi.org/10.1016/j.apcatb.2017.09.041.

References

[1] Y.F. Xu, M.Z. Yang, B.X. Chen, X.D. Wang, H.Y. Chen, D.B. Kuang, C.Y. Su, J. Am. Chem. Soc. 139 (2017) 5660–5663.
[2] A. Dhakshinamoorthy, A.M. Asiri, H. García, Angew. Chem. Int. Ed. 55 (2016) 5414–5445.
[3] Y. Zheng, L. Lin, B. Wang, X. Wang, Angew. Chem. Int. Ed. 54 (2015) 12868–12884.
[4] W.J. Ong, L.L. Tan, Y.H. Ng, S.T. Yong, S.P. Chai, Chem. Rev. 116 (2016) 7159–7329.
[5] J. Xu, Y. Wang, Y. Zhu, Langmuir 29 (2013) 10566–10572.
[6] G. Dong, L. Yang, F. Wang, L. Zang, C. Wang, ACS Catal. 6 (2016) 6511–6519.
[7] Q. Han, B. Wang, J. Gao, Z. Cheng, Y. Zhao, Z. Zhang, L. Qu, ACS Nano 10 (2016) 2745–2751.
[8] C. Ye, J.X. Li, Z.J. Li, X.B. Li, X.B. Fan, L.P. Zhang, B. Chen, C.H. Tung, L.Z. Wu, ACS Catal. 5 (2015) 6973–6979.
[9] P. Xia, B. Zhu, J. Yu, S. Cao, M. Jaroniec, J. Mater. Chem. A 5 (2017) 3230–3238.
[10] L. Yang, J. Huang, L. Shi, L. Cao, Q. Yu, Y. Jie, F. Jie, H. Ouyang, J. Ye, Appl. Catal. B Environ. 204 (2017) 335–345.
[11] H. Shi, G. Chen, C. Zhang, Z. Zou, ACS Catal. 4 (2014) 3637–3643.
[12] C. Pan, J. Xu, Y. Wang, D. Li, Y. Zhu, Adv. Funct. Mater. 22 (2012) 1518–1524.
[13] S. Kumar, T. Surendar, A. Baruah, V. Shanker, J. Mater. Chem. A 1 (2013) 5333–5340.

[14] Y. Wang, R. Shi, J. Lin, Y. Zhu, Energy Environ. Sci. 4 (2011) 2922–2929.
[15] S. Thaweesak, M. Lyu, P. Peerakiatkhajohn, T. Butburee, B. Luo, H. Chen, L. Wang, Appl. Catal. B Environ. 202 (2017) 184–190.
[16] X. Shi, M. Fujitsuka, Z. Lou, P. Zhang, T. Majima, J. Mater. Chem. A 5 (2017) 9671–9681.
[17] G. Zhang, S. Zang, X. Wang, ACS Catal. 5 (2015) 941–947.
[18] P. Ye, X. Liu, J. Iocozzia, Y. Yuan, L. Gu, G. Xu, Z. Lin, J. Mater. Chem. A 5 (2017) 8493–8498.
[19] M.T. Uddin, Y. Nicolas, C. Olivier, T. Toupance, L. Servant, M.M. Müller, H.J. Kleebe, J. Ziegler, W. Jaegermann, Inorg. Chem. 51 (2012) 7764–7773.
[20] X. Chen, B. Zhou, S. Yang, H. Wu, Y. Wu, L. Wu, J. Pan, X. Xiong, RSC Adv. 5 (2015) 68953–68963.
[21] Y. Zang, L. Li, X. Li, R. Lin, G. Li, Chem. Eng. J. 246 (2014) 277–286.
[22] L. Yang, J. Huang, L. Shi, L. Cao, W. Zhou, K. Chang, X. Meng, G. Liu, Y. Jie, J. Ye, Nano Energy 36 (2017) 331–340.
[23] S.N. Habisreutinger, L. Schmidt-Mende, J.K. Stolarczyk, Angew. Chem. Int. Ed. 52 (2013) 7372–7408.
[24] P. Li, Y. Lan, Q. Zhang, Z. Zhao, T. Pullerits, K. Zheng, Y. Zhou, J. Phys. Chem. C 120 (2016) 9253–9262.
[25] J. Sun, L. Xiao, S. Jiang, G. Li, Y. Huang, J. Geng, Chem. Mater. 27 (2015) 4594–4603.
[26] H. You, R. Liu, C. Liang, S. Yang, F. Wang, X. Lu, B. Ding, J. Mater. Chem. A 1 (2013) 4097–4104.
[27] L. Ran, D. Zhao, X. Gao, L. Yin, Cryst. Eng. Comm. 17 (2015) 4225–4237.
[28] L. Zhou, C. Zhao, B. Giri, P. Allen, X. Xu, H. Joshi, Y. Fan, L.V. Titova, P.M. Rao, Nano Lett. 16 (2016) 3463–3474.
[29] K. Peters, P. Zeller, G. Stefanic, V. Skoromets, H. Němec, P. Kužel, D. Fattakhova-Rohlfing, Chem. Mater. 27 (2015) 1090–1099.
[30] S. Ouyang, J. Ye, J. Am. Chem. Soc. 133 (2011) 7757–7763.
[31] H.Y. Jiang, P. Li, J.H. Ye, J.J. Lin, Mater. Chem. A 3 (2015) 5119–5125.
[32] J. Li, B. Shen, Z. Hong, B. Lin, B. Gao, Y. Chen, Chem. Commun. 48 (2012) 12017–12019.
[33] X. Lu, F. Yang, X. Geng, P. Xiao, Electrochim. Acta 147 (2014) 596–602.
[34] Z.F. Huang, J. Song, L. Pan, Z. Wang, X. Zhang, J.J. Zou, W. Mi, X. Zhang, Nano Energy 12 (2015) 646–656.
[35] S. Guo, Y. Zhu, Y. Yan, Y. Min, J. Fan, Q. Xu, Appl. Catal. B Environ. 185 (2016) 315–321.
[36] Y. Wu, T. Wang, Y. Zhang, S. Xin, X. He, D. Zhang, J. Shui, Sci. Rep. 6 (2016) 24314.
[37] L. Shi, T. Wang, H. Zhang, K. Chang, J. Ye, Adv. Funct. Mater. 25 (2015) 5360–5367.
[38] I.M. Mohamed, V.D. Dao, A.S. Yasin, H.M. Mousa, H.O. Mohamed, H.S. Choi, M.K. Hassan, N.A. Barakat, Chem. Eng. J. 304 (2016) 48–60.
[39] X. Li, D. Shao, H. Xu, W. Lv, W. Yan, Chem. Eng. J. 285 (2016) 1–10.
[40] Y. Guo, S. Song, Y. Zheng, R. Li, T. Peng, Dalton Trans. 45 (2016) 14071–14079.
[41] S. Ghosh, K. Das, K. Chakrabarti, S.K. De, Dalton Trans. 42 (2013) 3434–3446.
[42] R. Yin, Q. Luo, D. Wang, H. Sun, Y. Li, X. Li, J. An, J. Mater. Sci. 49 (2014) 6067–6073.
[43] E. Leblanc, L. Périer-Camby, G. Thomas, R. Gibert, M. Primet, P. Gelin, Sens. Actuators B Chem. 62 (2000) 67–72.
[44] L.R.B. Santos, T. Chartier, C. Pagnoux, J.F. Baumard, C.V. Santillii, S.H. Pulcinelli, A. Larbot, J. Europe. Ceram. Soc. 24 (2004) 3713–3721.
[45] W. Yu, D. Xu, T. Peng, J. Mater. Chem. A 3 (2015) 19936–19947.
[46] L. Shi, K. Chang, H. Zhang, X. Hai, L. Yang, T. Wang, J. Ye, Small 12 (2016) 4431–4439.
[47] P. Qiu, H. Chen, C. Xu, N. Zhou, F. Jiang, X. Wang, Y. Fu, J. Mater. Chem. A 3 (2015) 24237–24244.
[48] X. Lei, K. Yu, H. Li, Z. Tang, B. Guo, J. Li, H. Fu, Q. Zhang, Z. Zhu, J. Appl. Phys. 119 (2016) 154303.
[49] Y. Gu, Z. Jiao, M. Wu, B. Luo, Y. Lei, Y. Wang, L. Wang, H. Zhang, Nano Res. 10 (2017) 121–133.
[50] H. Luo, Z. Fang, N. Song, T. Garvey, R. Lopez, T.J. Meyer, ACS Appl. Mater. Interfaces 7 (2015) 25121–25128.
[51] C. Ke, W. Zhu, Z. Zhang, E.S. Tok, B. Ling, J. Pan, Sci. Rep. 5 (2015) 17424.
[52] Y. Hou, A.B. Laursen, J. Zhang, G. Zhang, Y. Zhu, X. Wang, S. Dahl, I. Chorkendorff, Angew. Chem. Int. Ed. 52 (2013) 3621–3625.
[53] F. Liao, Y. Huang, J. Ge, W. Zheng, K. Tedsree, P. Collier, X. Hong, S.C. Tsang, Angew. Chem. Int. Ed. 50 (2011) 2162–2165.
[54] F.A. Mir, K.M. Batoo, Appl. Phys. A 122 (2016) 1–7.
[55] L. Shi, T. Wang, H. Zhang, K. Chang, X. Meng, H. Liu, J. Ye, Adv. Sci. 2 (2015) 1500006.
[56] L. Yang, J. Huang, L. Cao, L. Shi, Q. Yu, X. Kong, Y. Jie, Sci. Rep. 6 (2016) 27765.
[57] Y. Li, S. Ouyang, H. Xu, X. Wang, Y. Bi, Y. Zhang, J. Ye, J. Am. Chem. Soc. 138 (2016) 13289–13297.
[58] L. Shi, P. Li, W. Zhou, T. Wang, K. Chang, H. Zhang, T. Kako, G. Liu, J. Ye, Nano Energy 28 (2016) 158–163.
[59] N. Tian, H. Huang, C. Liu, F. Dong, T. Zhang, X. Du, S. Yu, Y, J. Mater. Chem. A 3 (2015) 17120–17129.
[60] G. Liu, P. Niu, L. Yin, H.M. Cheng, J. Am. Chem. Soc. 134 (2012) 9070–9073.